Monthly Notices of the ROYAL ASTRONOMICAL SOCIETY

MNRAS **454,** 3073–3081 (2015) doi:10.1093/mnras/stv2195

Neutrino-driven explosions of ultra-stripped Type Ic supernovae generating binary neutron stars

Yudai Suwa,[1,2]★ Takashi Yoshida,[1,3] Masaru Shibata,[1] Hideyuki Umeda[3] and Koh Takahashi[3]

[1]*Yukawa Institute for Theoretical Physics, Kyoto University, Kitashirakawa Oiwake-cho, Sakyo-ku, Kyoto 606-8502, Japan*
[2]*Max-Planck-Institut für Astrophysik, Karl-Schwarzschild-Str. 1, D-85748 Garching, Germany*
[3]*Department of Astronomy, Graduate School of Science, University of Tokyo, Tokyo 113-0033, Japan*

Accepted 2015 September 21. Received 2015 September 21; in original form 2015 June 25

ABSTRACT

We study explosion characteristics of ultra-stripped supernovae (SNe), which are candidates of SNe generating binary neutron stars (NSs). As a first step, we perform stellar evolutionary simulations of bare carbon–oxygen cores of mass from 1.45 to 2.0 $M_\odot$ until the iron cores become unstable and start collapsing. We then perform axisymmetric hydrodynamics simulations with spectral neutrino transport using these stellar evolution outcomes as initial conditions. All models exhibit successful explosions driven by neutrino heating. The diagnostic explosion energy, ejecta mass, Ni mass, and NS mass are typically $\sim 10^{50}$ erg, $\sim 0.1\,M_\odot$, $\sim 0.01\,M_\odot$, and $\approx 1.3\,M_\odot$, which are compatible with observations of rapidly evolving and luminous transient such as SN 2005ek. We also find that the ultra-stripped SN is a candidate for producing the secondary low-mass NS in the observed compact binary NSs like PSR J0737−3039.

Key words: binaries: close – stars: evolution – stars: massive – stars: neutron – supernovae: general – supernovae: individual: SN 2005ek.

1 INTRODUCTION

Mergers of binary compact objects, i.e. neutron stars (NSs) and black holes (BHs), are promising candidates of strong gravitational wave (GW) sources. Event rates of these mergers are estimated based on the number of observed binary NSs in our galaxy and population synthesis calculations (e.g. Abadie et al. 2010). These estimates, however, have large uncertainty with, roughly speaking, two orders of magnitude. Recalling that the compact objects are formed through gravitational collapse and subsequent supernova (SN) explosions, there should be transient events generating binary compact objects observable by electromagnetic waves. SN surveys by currently working facilities e.g. the Subaru Hyper Suprime-Cam (Miyazaki et al. 2012; Tominaga et al. 2014), Palomar Transient Factory (Law et al. 2009; Rau et al. 2009), Catalina Real-Time Transient Survey (Drake et al. 2009), Panoramic Survey Telescope and Rapid Response System (Pan-STARRS1; Kaiser et al. 2010), and SkyMapper (Keller et al. 2007) and also by coming future projects (e.g. Large Synoptic Survey Telescope;[1] LSST) will be able to give constraints on the formation rate of transient objects including binary compact objects.

One of the possible candidates for an SN forming a close binary system is *ultra-stripped* SN (Tauris, Langer & Podsiadlowski 2015), which would launch peculiar Type Ib/c SN with a faint and fast decaying light curve. Peak luminosity of Type Ib/c SNe is determined primarily by the ejected mass of ^{56}Ni, $M_{^{56}\mathrm{Ni}}$, while the time-scale around the peak is determined by the diffusion time-scale $\tau_c \propto M_{\rm ej}^{3/4} E_{\rm K}^{-1/4}$, where $M_{\rm ej}$ is the ejecta mass and $E_{\rm K}$ is the kinetic energy of the ejecta (Arnett 1982). Therefore, the low peak luminosity and short characteristic time imply the small masses of the ejecta and ^{56}Ni. For instance, Type Ic SN 2005ek is one of these SNe (Drout et al. 2013; Tauris et al. 2013), whose estimated ejecta mass, $\sim O(0.1)\,M_\odot$, is notably smaller than typical SN Ic, $O(1)\,M_\odot$ (Drout et al. 2011), as well as smaller ^{56}Ni mass, and the explosion energy is also smaller by an order of magnitude ($O(10^{50})$ erg) than typical core-collapse SNe ($O(10^{51})$ erg). To model these rapidly evolving SNe with small ejecta mass, the progenitor stars are thought to be stripped much more than canonical stripped-envelope Type Ib/c SNe, that is, ultra-stripped SNe coined by Tauris et al. (2013, 2015). Besides SN 2005ek and other known SNe, 10 rapidly evolving transients were recently detected by Pan-STARRS1, which exhibit shorter decaying time-scale ($\sim$10 d) than canonical SNe with peak barometric luminosities ranging from $\sim 10^{42}$ to 10^{43} erg s^{-1} (Drout et al. 2014). These ultra-stripped SNe are conjectured as products of close binary systems that experienced strong binary interactions, e.g. common envelope phase, which result in close binary compact objects. Therefore, by

★ E-mail: suwa@yukawa.kyoto-u.ac.jp
[1] http://www.lsst.org/lsst/

Table 1. Properties of progenitor models.

Model	$M_{\rm CO}$ ($M_\odot$)	$M_{\rm ZAMS}{}^a$ ($M_\odot$)	$X_{\rm C}$	$X_{\rm O}$	Radius (10^4 km)	$\xi_{1.4}$	$M_{\rm Fe}{}^b$ ($M_\odot$)	$M_{\rm Fe}{}^c$ ($M_\odot$)	$M_{\rm env}$ ($10^{-3}\,M_\odot$)	$E_{\rm bind,\,env}$ (10^{48} erg)	$E^d_{\rm bind,He}$ (10^{49} erg)	$E_{\rm bind}$ (10^{50} erg)
CO145	1.45	9.75	0.360	0.611	1.28	0.468	1.33	1.32	4.80	2.28	0.1–1.3	3.97
CO145c	1.45	9.75	0.471	0.500	1.78	0.502	1.31	1.28	1.45	0.46	0.1–1.3	3.99
CO15	1.5	10.0	0.360	0.611	2.20	0.600	1.31	1.29	1.60	0.38	0.5–1.7	4.17
CO16	1.6	10.5	0.350	0.621	1.93	0.912	1.34	1.34	2.63	0.80	0.7–2.8	5.39
CO16c	1.6	10.5	0.471	0.500	1.73	0.850	1.36	1.34	2.42	0.95	0.7–2.8	4.69
CO18	1.8	11.5	0.350	0.621	2.64	0.851	1.35	1.37	8.09	2.20	1.2–3.8	4.92
CO20	2.0	12.8	0.330	0.641	3.66	0.968	1.37	1.37	8.48	1.66	2.2–4.7	5.72

[a]This is corresponding mass of ZAMS stars, which makes the same mass of CO core.
[b]The iron core mass is determined by the mass with the electron fraction of $Y_{\rm e} < 0.495$.
[c]The iron core mass is determined by the mass with the mass fraction of the element groups in $Z \geq 22$ (Ti-) larger than 0.5.
[d]These values are taken from fig. 15 in Tauris et al. (2015).

assuming that the order of the ultra-stripped SN rate is the same as that of the merger rate, we will be able to measure the merger rate through SN surveys. The current prediction of NS merger rate is between $\sim 10^{-6}$ and 4×10^{-3} galaxy^{-1} year^{-1} (Abadie et al. 2010), which is corresponding to $\sim$0.01 and 40 per cent of core-collapse SN rate ($\sim$0.01 galaxy^{-1} year^{-1}), while observed ultra-stripped SN rate would be $\sim$0.1–1 per cent of SNe (Tauris et al. 2015). After the detection of GWs, this conjecture can be tested using statistics of GW sources.

To predict the properties of these transient objects for coming LSST era, we investigate the explosion characteristics of the ultra-stripped SNe by means of numerical simulations. The current standard model of the explosion mechanism for core-collapse SNe is based on a neutrino-driven delayed explosion scenario (Colgate & White 1966; Bethe & Wilson 1985), in which copious amount of neutrinos emitted in the vicinity of a newly born NS are absorbed by the surrounding materials and they effectively act as heating (see Janka 2012; Kotake et al. 2012; Burrows 2013; Foglizzo et al. 2015, for latest reviews and references therein). In this study, we perform (i) stellar evolutionary simulations of bare carbon and oxygen (CO) cores without massive hydrogen and helium envelopes, which would be possible consequences of close binary interactions such as common envelope phase, until iron cores form and (ii) axisymmetric neutrino-radiation hydrodynamics simulations to investigate their explosions. The paper is organized as follows. Section 2 describes our stellar evolutionary simulations and stellar structure just prior to the collapse. The numerical method of following hydrodynamics simulations and the results are presented in Section 3. We summarize our results and discuss their implications in Section 4.

2 STELLAR EVOLUTION AND PROGENITOR STRUCTURES

Here, we describe the evolution of CO cores obtained in this study. To make initial conditions for hydrodynamics simulations, we first perform stellar evolutionary simulations of CO cores with masses of 1.45, 1.5, 1.6, 1.8, and 2.0 $M_\odot$ supposing that stellar mass loss has already occurred by their hypothetical companion NSs. By removing stellar envelope, the stellar evolutionary simulations are done with a code described in Umeda, Yoshida & Takahashi (2012), Takahashi, Yoshida & Umeda (2013) and Yoshida, Okita & Umeda (2014). The nuclear reaction network consists of 300 species of nuclei (Takahashi et al. 2013; Yoshida et al. 2014). Schwarzschild criterion is employed as the convection criterion and the convective mixing of the chemical composition is evolved using diffusion equation. We also take into account thermohaline mixing (e.g. Siess 2009) and the diffusion coefficient is adopted from equation 2 in Siess (2009). The initial chemical compositions of the CO cores are evaluated by those after the He burning with the metallicity $Z = 0.02$. Since the C/O ratio of the core depends on the stellar mass, we assume the mass fractions of ^{12}C and ^{16}O, which are listed in Table 1.

It is quite difficult to relate between zero-age main-sequence (ZAMS) mass and CO-core mass in binary systems because mass transfer proceeds very complicatedly during the evolution. On He star–NS binaries, He stars with $M_{\rm He} \lesssim 3.5\,M_\odot$ and with the initial orbital period of $P_{\rm orb} \lesssim 0.5$ d have an evolutional path to ultra-stripped SNe (Tauris et al. 2015). These He stars evolved to CO cores with $M_{\rm CO} \lesssim 1.8\,M_\odot$ surrounded by very thin He envelope. Thus, the mass range of our CO-core models is adequate for the progenitors of ultra-stripped SNe. For comparison, we list the stellar mass at the zero-age main sequence (ZAMS), $M_{\rm ZAMS}$, which makes the similar CO core as shown in Table 1. The mass range of the He cores is 2.6–3.3 $M_\odot$. These values are evaluated based on the evolution of 9–15 $M_\odot$ stars up to the Ne ignition or the central C exhaustion (see also Woosley & Heger 2015). We assume the convective overshooting as a diffusion process until the core He burning in these calculations. The diffusion coefficient is adopted from equation 2 in Herwig (2000) and the parameter on the scaleheight f is set to be 0.01.

We continue evolutionary simulations until the iron cores become unstable and start collapsing. Here we briefly explain the evolution of our models. More details will be shown in Yoshida et al. (in preparation). Fig. 1 shows the evolution of the central temperature ($T_{\rm C}$) and density ($\rho_{\rm C}$) of CO145, CO16, and CO20 models. Here, the units of $T_{\rm C}$ and $\rho_{\rm C}$ are kelvin and g cm^{-3}, respectively. Fig. 2 is the Kippenhahn diagram of CO145 model, which displays the time evolution of convective regions and the energy generation inside the star. Although all models finally form Fe cores, the evolution paths depend on the CO-core mass. In CO145 model, off-centre Ne burning is ignited (Ne-flash) after several C-shell burnings (label *a* in Figs 1 and 2). The following O burning is also ignited at an off-centre region (label *b*). Then, the burning front gradually moves into the centre and the temperature at the front increases. When the central density reaches $\log \rho_{\rm C} \sim 8.2$, Si burning is ignited at the burning front and the convective layer extends to $M_r \sim 0.9\,M_\odot$ (label *c*). The burning front continues to move inwards and the O/Ne-enriched material in the central region is burned to Fe-peak

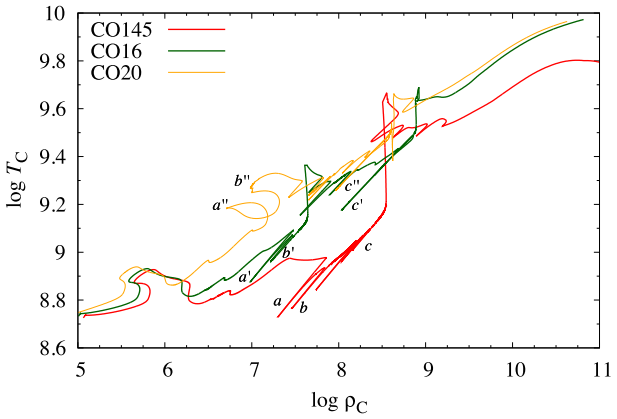

Figure 1. Evolutionary path in the plane of the central density and temperature of CO145 (red line), CO16 (green line), and CO20 (orange line) models. Labels a and a', b and b', and c, c', and c'' correspond to the off-centre Ne, O, and Si burnings, respectively. Labels a'' and b'' denote the central Ne and O burnings.

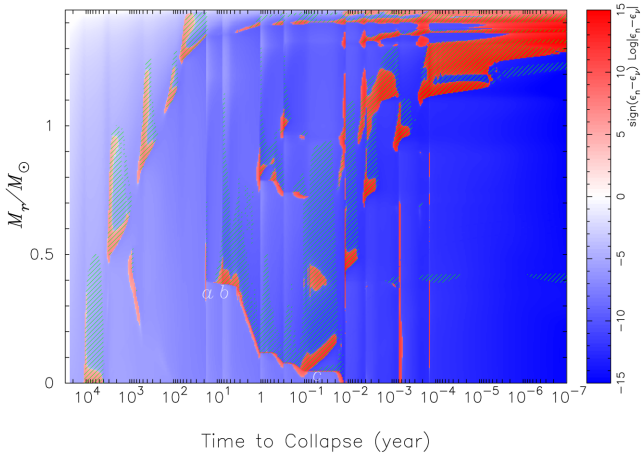

Figure 2. Kippenhahn diagram of CO145 model. Green-hatched areas indicate convective regions. Labels a, b, and c correspond to the off-centre Ne, O, and Si burnings at 17.1 yr, 10.7 yr, and 38.8 d before core collapse.

elements. When the central density reaches $\log \rho_C \sim 8.5$, the burning front reaches the centre and the central temperature rises steeply. The Fe core grows up to $\sim$0.5 $M_\odot$ after the burning front reaches the centre. Then, Si-shell burning occurs and the Fe core grows up further, and finally, the core collapses.

CO16 model evolves on a different evolution track as shown in Fig. 1. After the Ne-flash (label a') and off-centre O burning (label b'), the burning front reaches the centre. As a result, the Si core with 0.6 $M_\odot$ is formed and it grows up by O-shell burnings. Then, the Si-flash occurs at $M_r = 0.03\,M_\odot$ (label c'). The Si-flash forms large convective region up to $M_r \sim 1.1\,M_\odot$ above the burning front. After that, Si-shell burnings also follow. The burning front again gradually moves inwards and finally reaches the centre after the second Si-shell burning. Finally, the Fe core grows to 1.34 $M_\odot$ and collapses. The evolution of CO15 model is similar to that of CO16. The Ne-flash and Si-flash occur at higher central density.

The evolution of CO20 model is similar to those of massive stars that collapse to normal SNe until O-shell burning. Ne and O burnings are ignited at the centre and the convective core forms (labels a'' and b''). The Ne- and O-shell burnings extend the central Si core after O-core burning. However, Si burning starts at an off-centre region when the central density reaches $\log \rho_C \sim 8.6$ (label c''). The off-centre Si burning forms a large convective region to 1.2 $M_\odot$. The burning front moves inwards and reaches the centre during Si-shell burning. Finally, a 1.37 $M_\odot$ Fe core is formed, and then, it collapses. The evolution of CO18 model is similar to CO20 model, i.e. Ne and O are ignited at the centre and Si ignites at an off-centre region. The central density at the ignition of off-centre Si burning is higher than that of CO20.

We note that recently the evolution of 9–11 $M_\odot$ stars has been investigated in Woosley & Heger (2015). Since they considered artificial energy deposition to the cooler underlying zone of the off-centre burning front, the burning front rapidly moved inwards. We do not consider this effect, but we instead set larger coefficient value of thermohaline mixing. In CO145 model, the central contraction makes the temperature at the burning front high enough to ignite Si before the front reaches the centre. Even so, CO145 model forms an Fe core. Although the inward motion of the burning front depends on the instability at the base of the burning front and has uncertainty, we expect that the stars igniting Ne-flash will form an Fe core and collapse.

The mass fraction distributions of CO145 and CO16 models at the final step of the stellar evolution simulations are shown in Fig. 3. These models consist of 1.33 and 1.34 $M_\odot$ Fe cores surrounded by thin Si, O/Si, O/Ne, and O/C layers. Composition-inverted layers have been seen during the Ne-flash and Si-flash. The composition inversion has been removed during the inward motion of the burning front. We do not see large differences in Fe core masses in our CO-core models (see Table 1).

We assume the mass fractions of C and O in the CO cores based on the results of single-star models. In the case of binary evolution, ultra-stripped CO cores have lost the H-rich envelope before or during the early phase of the He-core burning. Stripping the H-rich envelope prevents the growth of He core and shortens the time-scale of the He-core burning. Thus, the C/O ratio of an ultra-stripped CO core is larger than the CO core in single stars (Brown et al. 2001). Wellstein & Langer (1999) investigated the evolution of various binary systems of massive stars. They obtained that a binary system consisting of 13 and 12 $M_\odot$ stars with an initial orbital period of 3.1 d experiences Case B+BB mass transfer and the primary star becomes a 1.42 $M_\odot$ He star with CO-core mass being 1.31 $M_\odot$ and the central carbon mass fraction being 0.40.

We calculate the evolution of 1.45 and 1.6 $M_\odot$ CO-core models with a large C/O ratio to investigate the C/O-ratio dependence of ultra-stripped SN progenitors. We set the mass fractions of C and O in these models to be 0.471 and 0.500, respectively. Properties of the models are shown as CO145c and CO16c in Table 1. We do not see large systematic differences between normal and large C/O-ratio models. CO145c model has an Fe core slightly smaller than CO145, while the Fe core of CO16c is slightly larger than that of CO16 for the criterion that the Fe core is determined by the electron fraction smaller than 0.495. The difference of the compactness parameter between the normal model and large C/O-ratio model is within 10 per cent. We consider that properties of ultra-stripped SN progenitor do not strongly depend on the C/O ratio. It should be noted that the evolution of the central region of the CO cores depends on the C/O ratio. The convective regions of the C-core or C-shell burnings become large in the models of the large C/O ratio. In CO145c model, Ne is ignited at 0.35 $M_\odot$ in the mass coordinates. The Ne/O-burning front reaches the centre before the Si ignition. Then, Si is ignited at 0.04 $M_\odot$. In CO16c model, Si burning occurs at the centre as a flash and, then, it turns to steady burning. Nevertheless, we do not see large difference by the C/O

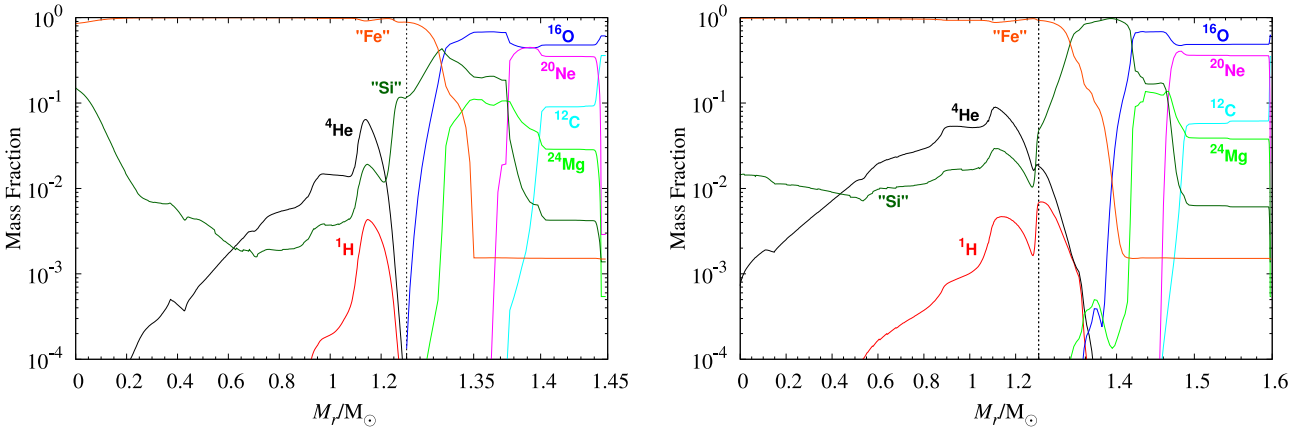

Figure 3. Mass fraction distributions of CO145 (left) and CO16 (right) models. Red, black, sky-blue, blue, pink, yellow-green, green, and orange lines correspond to ^{1}H, ^{4}He, ^{12}C, ^{16}O, ^{20}Ne, ^{24}Mg, "Si", and "Fe". "Si" and "Fe" indicate the element groups in $Z = 14$–21 (Si-Sc) and $Z \geq 22$ (Ti-), respectively. The scale of the horizontal axis changes at 1.3 $M_\odot$.

ratio in the region where the structures and composition are mainly determined by the Si-shell burning. Once the Fe core is formed by the central or off-centre Si burning, the core grows through the following Si-shell burning. Thus, we consider that properties of SN progenitors such as Fe core mass and compactness parameter are insensitive to the C/O ratio.

These CO cores have a thin CO envelope where C-shell burnings scarcely affect the composition. We listed the masses of the envelope, $M_{\rm env}$, which the convective region did not reach during C-shell burnings, and their binding energy, $E_{\rm bind,\,env}$, in Table 1. The envelope mass is less than 0.01 $M_\odot$ for all the models. The binding energy of the envelope is (0.4–2) $\times 10^{48}$ erg, which is smaller than 1 per cent of the binding energy of the whole star ($E_{\rm bind}$, see Table 1).

Although we do not take into account He-rich envelope, the progenitors of ultra-stripped SNe in NS binary systems could have the envelope (Tauris et al. 2013, 2015). Tauris et al. (2015) showed the dependence of the He mass and the binding energy of the He envelope on the final CO-core mass. Here, we estimate the binding energy of the He envelope from fig. 15 in Tauris et al. (2015) and from their discussion that the He mass is smaller than 0.2 $M_\odot$ (see section 4.1.1 in Tauris et al. 2015). The estimated range of the envelope is listed in Table 1. The binding energy of the He envelope is at most several times 10^{49} erg. Thus, we expect that the envelope has a small contribution in the binding energy for ultra-stripped SNe.

Fig. 4 presents density structures at the end of evolutionary simulations. More detailed properties are summarized in Table 1. Following O'Connor & Ott (2011), we define the compactness parameter, ξ_M, by

$$\xi_M = \frac{M/M_\odot}{R(M)/1000\ {\rm km}}, \quad (1)$$

where $R(M)$ is the radius with M being mass enclosed inside R. We employ $\xi_{1.4}$, which is measured by $M_r = 1.4\,M_\odot$. Note that other groups have employed different values such as $\xi_{2.5}$, $\xi_{1.75}$, and $\xi_{1.5}$ (O'Connor & Ott 2011, 2013; Ugliano et al. 2012; Nakamura et al. 2014; Sukhbold & Woosley 2014; Pejcha & Thompson 2015). Since our models have small CO-core mass, we rely on a different parameter. Note also that in the original definition by O'Connor & Ott (2011), ξ is measured at the time of bounce. Later, Sukhbold & Woosley (2014) suggested that ξ measured just prior to collapse correlates with ξ at bounce. Hence, in this paper we evaluate ξ

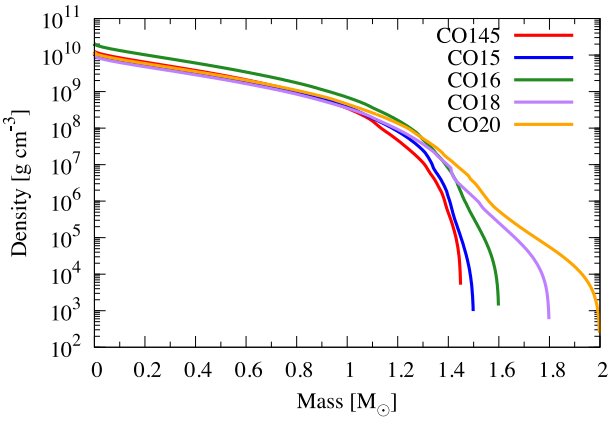

Figure 4. Density structure of CO cores at pre-collapse phase as a function of mass coordinate. Red, blue, green, purple, and orange lines represent models with CO cores of 1.45, 1.5, 1.6, 1.8, and 2.0 $M_\odot$, respectively.

with the pre-collapse density structures. We show two different definitions of the iron core mass, $M_{\rm Fe}$: one is based on the electron fraction and the other on mass fraction of heavy elements. The iron core mass does not depend strongly on CO-core mass since, broadly speaking, the core collapse sets in when the iron core mass exceeds Chandrasekhar mass (Baron & Cooperstein 1990).

3 HYDRODYNAMICS SIMULATIONS

3.1 Numerical methods

For the hydrodynamics simulations, we employ a two-dimensional (2D) neutrino-radiation hydrodynamics code, which is developed and used for investigating SN explosion mechanism (Suwa et al. 2010, 2011, 2013, 2014; Suwa 2014). With ZEUS-2D code (Stone & Norman 1992) as a base for the solver of hydrodynamics, we employ an equation of state of Lattimer & Swesty (1991) with an incompressibility $K = 220$ MeV and solve the spectral transfer of neutrinos by the isotropic diffusion source approximation scheme (Liebendörfer, Whitehouse & Fischer 2009) that splits the neutrino distribution function into two components, both of which are solved by using separate numerical techniques. Weak interaction rates are implemented following Bruenn (1985). We solve transfer

of electron-type neutrinos (ν_e) and antineutrinos ($\bar{\nu}_e$), but heavier leptonic neutrinos are not taken into account. In our 2D simulations, axial symmetry is assumed and 'ray-by-ray-plus' approach is implemented for multi-dimensional treatment of neutrino transfer (Buras et al. 2006). Spherical coordinates (r, θ) with logarithmic zoning in the radial direction and constant zoning in θ are used. The simulations are performed on a grid of 300 radial zones extending up to 5000 km with the smallest grid width being 1 km at the centre and 128 equidistant angular zones covering $0 < \theta < \pi$ for 2D simulations. For neutrino transport, we use 20 logarithmically spaced energy bins ranging from 3 to 300 MeV.

Note that at the current moment there is no complete model for the explosion mechanism of core-collapse SNe despite the long-lasting efforts. Recent multi-dimensional simulations of neutrino-radiation hydrodynamics have shown diversity of numerical results (e.g. Bruenn et al. 2013; Suwa et al. 2014; Dolence, Burrows & Zhang 2015; Melson et al. 2015b, used the same progenitor models and obtained different results). In addition, most exploding simulations exhibited order of magnitude smaller explosion energy than observation, and remnant compact objects often gained mass above the maximum mass of an NS, which would collapse to BHs instead of NSs.

We speculate, however, that all these implementations could universally reproduce ultra-stripped SNe. The reason for this speculation is that typical explosion energy of the ultra-stripped SNe is smaller ($O(10^{50})$ erg) than canonical SNe ($O(10^{51})$ erg), that is, stellar structures of progenitors for these different kinds of SNe are different. The explosion energy is determined naively by the binding energy of progenitor layers in the vicinity of mass cut (remnant compact object) so that stars with small binding energy are possible candidates of the weak explosions. This hypothesis was already applied for explanation of Type IIn-P SNe like SN 2009kn, which exhibit narrow emission lines, a short plateau phase in light curve, and small amount of ^{56}Ni. These observational features were reproduced by an electron-capture SN model, in which the progenitor star consists of an O-Ne-Mg degenerated core and a very thin envelope, giving the small explosion energy of $\sim 10^{50}$ erg (Moriya et al. 2014 based on the explosion simulation by Kitaura, Janka & Hillebrandt 2006). As we will show in the following subsection, we obtain explosion energy of $O(10^{50})$ erg, which is the same order of magnitude as the binding energy exterior to a remnant compact object at pre-collapse phase. We infer that even if we could perform *a realistic simulation* that would reproduce canonical explosion energy for canonical SN progenitors, the results obtained with weakly bound progenitors will be a weak explosion with its energy $\sim 10^{50}$ erg. Since the explosion energy of such simulations, however, could be larger than that of ours, it is safe to consider that our results give at least a lower limit of the explosion energy.

At first, we perform spherically symmetric (1D) simulations up to 5 ms after the bounce, which is determined by the largest central density, and 2D simulations follow them. Note that all 1D simulations fail to explode even when we continue simulations until several hundred milliseconds after the bounce.[2]

[2] Note that recent studies of full three-dimensional (3D) hydrodynamics simulations showed that 2D simulations are more favourable for explosion than those of 3D (see e.g. Hanke et al. 2013; Takiwaki, Kotake & Suwa 2014) so that we should note that the 2D simulations would optimize the conditions for successful explosions (but see also Melson, Janka & Marek 2015a).

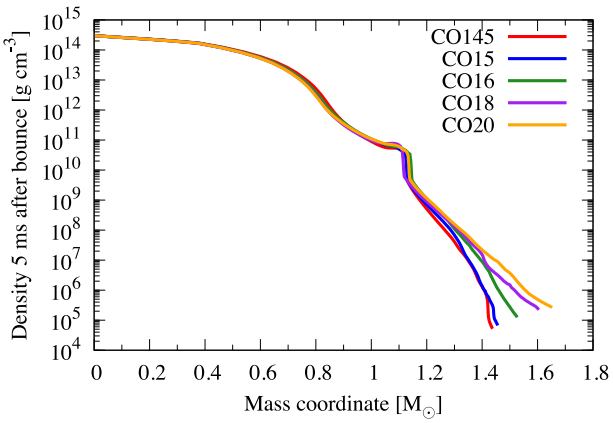

Figure 5. Density profiles at 5 ms after bounce. Line colours show the same models as Fig. 4.

3.2 Results

We show the density profiles at 5 ms after the bounce in Fig. 5. One can find that the density profiles of $M_r \lesssim 1.1\,M_\odot$ depend only weakly on the CO-core mass, but above this mass coordinate they differ from each other due to the different progenitor structure. This difference leads to different evolution of shocks, which is described in the following. Note that the density at a certain mass coordinate above $\sim 1.1\,M_\odot$ monotonically increases with the CO-core mass.

Fig. 6 presents evolution of entropy (left halves) and radial velocity (right halves) distributions at 100 (top-left panel), 200 (top-right), 250 (bottom-left), and 350 ms (bottom-right) after the bounce for model CO15. After core bounce, convective motion sets in initially due to an unstable entropy configuration (prompt convection) and subsequently due to neutrino heating in the gain region (neutrino-driven convection), but shock morphology is maintained to be approximately spherically symmetric (see the top-left panel). As the turbulent motion is further enhanced by the neutrino heating, the shock is deformed from spherical symmetry (see the top-right panel). Once the post-shock pressure (thermal pressure and turbulent pressure) overwhelms the ram pressure above the shock, the shock starts expanding and an explosion is launched. In this model, the expanding shock is rather spherical since the small envelope mass results in a small mass accretion rate on to the shock and small-scale convection dominates over large-scale motion driven by the standing accretion shock instability (SASI; Blondin, Mezzacappa & DeMarino 2003). This leads to a small kick velocity of protoneutron stars (PNS). One can observe a cold downflow on to the PNS even after the onset of the explosion (see an isolated blue region in the bottom-right panel of Fig. 6), which could increase the PNS mass. This downflow, however, has a small solid angle and the mass accretion rate is considerably small. Thus, the mass accreting on to the PNS at this moment is negligible. The PNS mass evolution will be discussed later.

Shock evolution processes in all 2D simulations are presented in Fig. 7. One can see that the three small mass models (CO145, CO15, and CO16) explode approximately at identical time, while more massive cores show later explosion. This is a consequence of the different envelope mass on the iron core. The early exploding models have clear phase transition from a slowly expanding phase to a rapidly exploding phase at $\sim$200 ms after the bounce. On the other hand, late exploding models show oscillations of the shock radius before the explosion. This is due to convection and SASI. The difference in the onset time of the explosion is a result of different

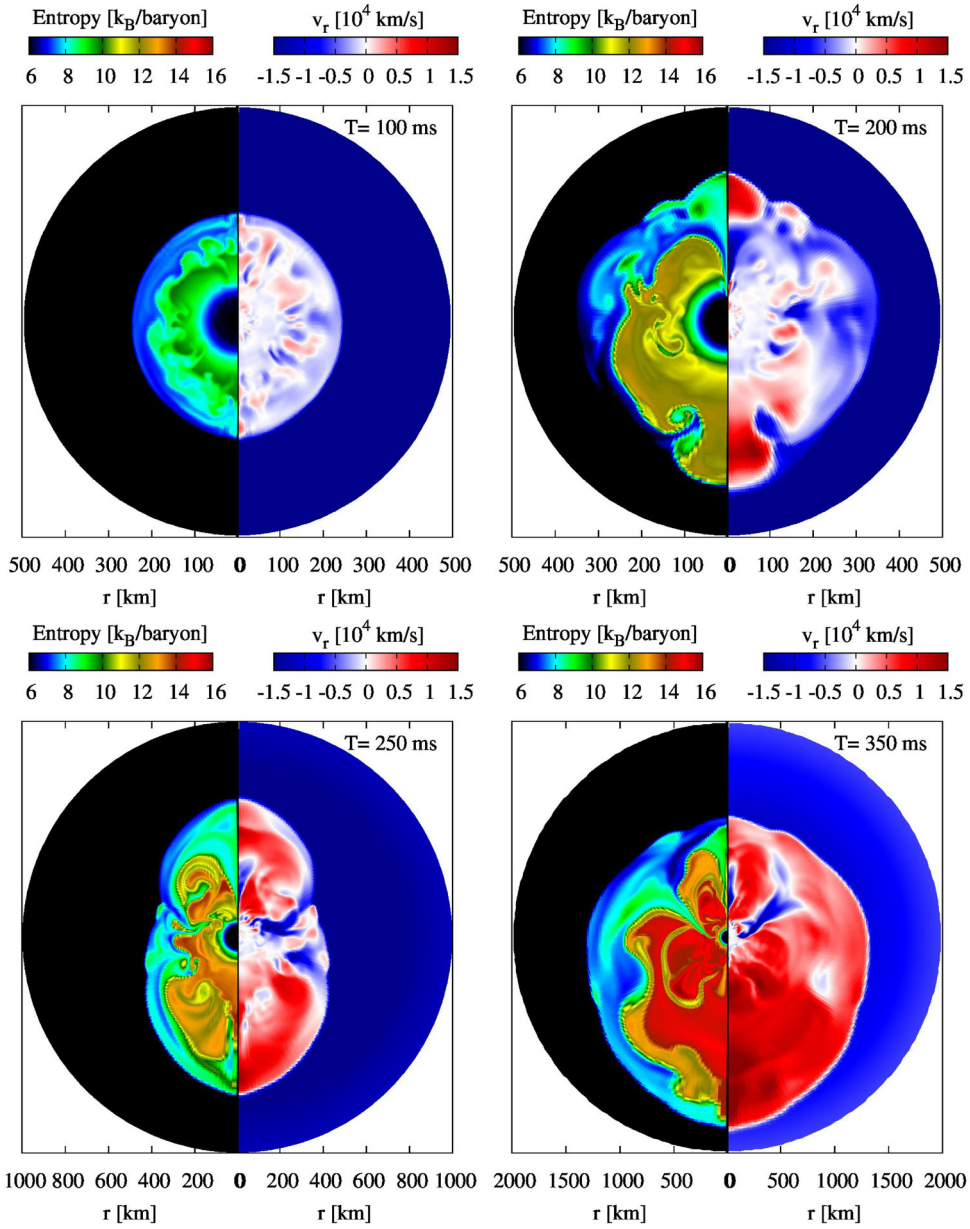

Figure 6. Specific entropy (in units of k_B baryon^{-1}; left halves of the individual panels) and radial velocity (in units of 10^4 km s^{-1}; right halves) profiles at 100 (top-left panel), 200 (top-right), 250 (bottom-left), and 350 ms (bottom-right) after the bounce for model CO15. In the entropy plots, bluish (reddish) colours represent small (large) entropy. In velocity plots, red region is expanding (positive radial velocity) and blue region is accreting (negative radial velocity).

mass accretion rate evolution due to the different envelope structure (see Fig. 5). The later onset of the explosion leads to larger PNS mass as shown in Fig. 8. Here we define PNS as the region with density above 10^{11} g cm^{-3}. CO145 and CO15 models form a PNS of baryonic mass $\approx$1.35 $M_\odot$, while other models give larger PNS mass.

In Table 2, we summarize results of our hydrodynamics simulations. $t_{\rm final}$ denotes the final post-bounce time of each simulation. The quantities listed in other columns are all measured at $t_{\rm final}$. $R_{\rm sh}$ is the angle-averaged shock radius, $E_{\rm exp}$ is diagnostic explosion energy, which is defined as the integral of the sum of specific internal, kinetic, and gravitational energies over all zones with positive value, $M_{\rm NS,\,baryon}$ is baryonic mass of the remnant NS calculated by integration over grid of $\rho > 10^{11}$ g cm^{-3}, $M_{\rm NS,\,grav}$ is the corresponding gravitational mass, $M_{\rm ej} = M_{\rm CO} - M_{\rm NS,\,baryon}$ is the ejecta mass, $M_{^{56}\rm Ni}$ is mass of ^{56}Ni, and $v_{\rm kick}$ is the estimated kick velocity of NSs. Note that these quantities are not the final outcome of the simulations, since all the simulations were terminated before the system relaxes to a stationary state to save the computational time. The gravitational mass is calculated by the baryonic mass using the following relation (Timmes, Woosley & Weaver 1996)

$$\frac{M_{\rm baryon}}{M_\odot} - \frac{M_{\rm grav}}{M_\odot} = 0.075 \left(\frac{M_{\rm grav}}{M_\odot}\right)^2. \quad (2)$$

^{56}Ni mass is calculated using tracer particle method (e.g. Nagataki et al. 1997). We assume that the mass elements with the maximum temperature being over 5×10^9 K achieve nuclear statistical equilibrium and synthesize ^{56}Ni completely. This gives just an approximate estimate. For more realistic calculation, we need to perform

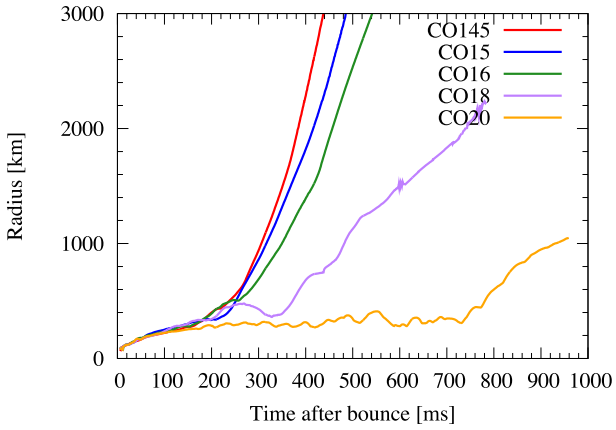

Figure 7. Evolutions of the radius of shocks.

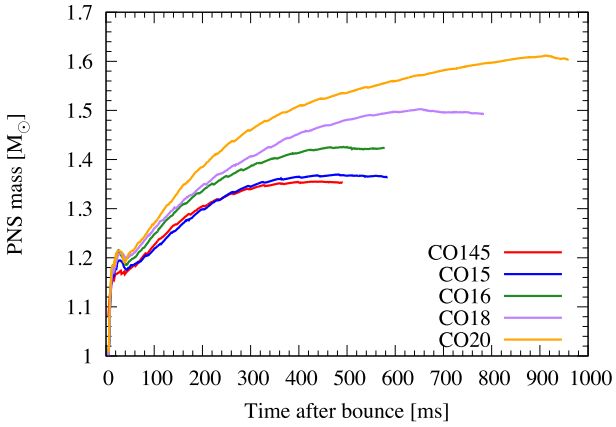

Figure 8. Time evolutions of PNS mass (defined by $\rho > 10^{11}$ g cm^{-3}).

detailed nucleosynthesis calculation, which is beyond the scope of this paper. The NS kick velocity is estimated by assuming the linear momentum conservation of the whole progenitor star, i.e. assuming that anisotropic mass ejection leads to NS kick (e.g. Wongwathanarat, Janka & Müller 2013). The linear momentum of ejecta is calculated by

$$\boldsymbol{P}_{\rm ej} = \int_{\rho<10^{11}\ {\rm g\ cm^{-3}}, v_r>0} \rho \boldsymbol{v} {\rm d}V, \quad (3)$$

where $\boldsymbol{v}$ is the velocity vector and v_r is its radial component. The NS kick velocity is then given by $\boldsymbol{v}_{\rm kick} = -\boldsymbol{P}_{\rm ej}/M_{\rm NS,baryon}$. Since the axial symmetry is assumed in our simulations, the kick velocity may be overestimated due to the existence of preferable direction of NS kick, i.e. symmetry axis. Additionally, the stochastic nature of post-shock turbulent flow would also change the degree of asymmetry of ejecta so that the initial small perturbation could change the kick velocity significantly (Scheck et al. 2006). More statistical study is needed to pin down this issue. It can be argued that small envelope, not small iron core itself, which can rapidly accelerate shock, would generally lead to small kick velocity due to too short time for SASI to build up (see also, e.g., Podsiadlowski et al. 2004; Bogomazov, Lipunov & Tutukov 2007).

4 SUMMARY AND DISCUSSION

We have performed both stellar evolution simulations of bare CO cores and explosion simulations for the end product of the CO cores for modelling ultra-stripped Type Ic SNe. We have found that all CO cores with mass from 1.45 to 2.0 $M_\odot$ resulted in explosion with energy of $O(10^{50})$ erg, which left NSs with gravitational mass from ∼1.24 to 1.44 $M_\odot$ and ejecta from ∼0.1 to 0.4 $M_\odot$ with synthesized ^{56}Ni of $O(10^{-2})\,M_\odot$. These values are compatible with observations of ultra-stripped SN candidates (Drout et al. 2013; Tauris et al. 2013, 2015). For SN 2005ek, $M_{\rm ej} \approx 0.2$–0.7 $M_\odot$ and $M_{\rm Ni} \approx 0.02$–0.05 $M_\odot$ are appropriate to fit its light curve. The event rate of these SNe is estimated as ∼1 per cent of core-collapse SN rate (Drout et al. 2013, 2014), which is also compatible with an NS merger rate estimation (Abadie et al. 2010).

We took a different approach from previous studies on ultra-stripped SNe (Tauris et al. 2013, 2015). In previous works, they self-consistently performed stellar evolutionary simulations until oxygen burning phase with self-consistent mass-loss driven by wind but explosion calculations were based on phenomenological modelling with three free parameters: kinetic energy of SN, Ni mass, and mass cut (i.e. NS mass). Based on this model, they found that ultra-stripped SN model could account for the light curve of SN 2005ek quite well. In our work, on the other hand, we performed stellar evolutionary simulations until the last phase of evolution, i.e. iron core collapse, but for initially bare CO cores without mass-loss. For the explosion phase, we performed neutrino-radiation hydrodynamics simulations to calculate explosion energy, Ni mass, and NS baryon mass in self-consistent manner. In this sense, this work is

Table 2. Summary of simulation results.

Model	$t_{\rm final}$[a] (ms)	$R_{\rm sh}$[b] (km)	$E_{\rm exp}$[c] (B)	$M_{\rm NS,\,baryon}$[d] ($M_\odot$)	$M_{\rm NS,\,grav}$[e] ($M_\odot$)	$M_{\rm ej}$[f] ($10^{-1}\,M_\odot$)	$M_{\rm Ni}$[g] ($10^{-2}\,M_\odot$)	$v_{\rm kick}$[h] (km s^{-1})
CO145	491	4220	0.177	1.35	1.24	0.973	3.54	3.20
CO15	584	4640	0.153	1.36	1.24	1.36	3.39	75.1
CO16	578	3430	0.124	1.42	1.29	1.76	2.90	47.6
CO18	784	2230	0.120	1.49	1.35	3.07	2.56	36.7
CO20[i]	959	1050	0.0524	1.60	1.44	3.95	0.782	10.5

Notes. [a]The final time of simulations measured by post-bounce time.
[b]The angle-averaged shock radius at $t_{\rm final}$.
[c]The explosion energy in units of B (=10^{51} erg) at $t_{\rm final}$, which is still increasing.
[d]The baryonic mass of NS at $t_{\rm final}$.
[e]The gravitational mass of NS computed by equation (2) at $t_{\rm final}$.
[f]The ejecta mass at $t_{\rm final}$.
[g]The Ni mass at $t_{\rm final}$.
[h]The kick velocity at $t_{\rm final}$.
[i]Note that this model is marginally exploding.

complementary to previous works. We found that outcomes of our hydrodynamics simulations for CO145, CO15, and CO16 are close to model parameters of Tauris et al. (2013) that well fit light curve of SN 2005ek ($M_{\rm NS} = 1.3\,{\rm M}_\odot$, $M_{\rm ej} = 0.2\,{\rm M}_\odot$, $E_{\rm exp} = 5 \times 10^{50}$ erg, and $M_{\rm Ni} = 0.05\,{\rm M}_\odot$). The light curve calculated with our hydrodynamical models will be presented in the forthcoming paper.

For CO145, CO15, CO16, and CO18 models, the baryon mass of the remnant NSs is in the range between 1.35 and 1.49 $\rm M_\odot$. The corresponding gravitational mass is 1.24–1.35 $\rm M_\odot$ for this baryon mass range depending only weakly on equations of state for NSs hypothetically employed. These values for the gravitational mass agree well with those for secondary NSs in observed compact binary systems (Lattimer 2012). This suggests that such secondary NSs may be formed from ultra-stripped SNe.

We showed that 1.45–2.0 $\rm M_\odot$ CO star models ignite Ne at the centre or an off-centre region. They form an Fe core and none of them evolve to electron-capture SN. Thus, the upper limit of the CO-core mass for electron-capture SN should be less than 1.45 $\rm M_\odot$. Tauris et al. (2015) adopted $M_{\rm ONe,\,f} = 1.43\,{\rm M}_\odot$ as an approximate upper limit for electron-capture SN. In the case of single-star evolution in Takahashi et al. (2013), a 10.8 $\rm M_\odot$ model ends its evolution as an electron-capture SN and an 11.0 $\rm M_\odot$ model ignites Ne at an off-centre region. Off-centre Ne ignition and gradual increase in the central temperature around the central density $\rho_{\rm C} \sim 10^9$ g cm^{-3} could be predictions of the Fe core formation and core-collapse SN. The evolution of CO cores less massive than 1.45 $\rm M_\odot$ will be shown in the forthcoming paper (Yoshida et al. in preparation).

Finally, we discuss the eccentricity of the binary system formed after the SN that leaves a secondary NS. Due to the mass ejection from the system, the binary system obtains the eccentricity, e, after the SN explosion. The eccentricity can be evaluated by (Bhattacharya & van den Heuvel 1991)

$$e = \frac{M_1^i - M_1^f}{M_1^f + M_{\rm NS}}, \tag{4}$$

where M_1 is the mass of exploding star before (after) the explosion indicated as i (f) and $M_{\rm NS}$ is the mass of the primary NS. Here, we assumed that the mass ejection occurs quickly and during the explosion the positions of these stars do not change. By giving the ejected mass, $M_{\rm ej} = M_1^i - M_1^f = 0.3\,{\rm M}_\odot$ and $M_1^f = M_{\rm NS} = 1.3\,{\rm M}_\odot$, we get $e \approx 0.12$, which is compatible with one of observed binary NSs, J0737−3039, whose current eccentricity is 0.088 and estimated eccentricity at birth of second pulsar is 0.11 (Piran & Shaviv 2005). The small centre-of-mass velocity of this system also implies a small ejecta mass and slow pulsar kick (Dall'Osso, Piran & Shaviv 2014).

ACKNOWLEDGEMENTS

We thank A. Wongwathanarat, M. Tanaka, and T. Moriya for discussions. We also appreciate comments on an earlier draft of this paper by E. Müller, T. Piran, T. Tauris, and A. Tutukov. YS thanks the Max Planck Institute for Astrophysics for its hospitality. Numerical computations in this study were in part carried out on XC30 at CfCA in NAOJ and SR16000 at YITP in Kyoto University. YS was supported by Japan Society for the Promotion of Science (JSPS) postdoctoral fellowships for research abroad. KT was supported by research fellowships of JSPS for Young Scientists. This study was also supported in part by the Grant-in-Aid for Scientific Research (Nos. 24244028, 26400220, and 26400271), MEXT SPIRE, and JICFuS.

REFERENCES

Abadie J. et al., 2010, Class. Quantum Grav., 27, 173001
Arnett W. D., 1982, ApJ, 253, 785
Baron E., Cooperstein J., 1990, ApJ, 353, 597
Bethe H. A., Wilson J. R., 1985, ApJ, 295, 14
Bhattacharya D., van den Heuvel E. P. J., 1991, Phys. Rep., 203, 1
Blondin J. M., Mezzacappa A., DeMarino C., 2003, ApJ, 584, 971
Bogomazov A. I., Lipunov V. M., Tutukov A. V., 2007, Astron. Rep., 51, 308
Brown G. E., Heger A., Langer N., Lee C.-H., Wellstein S., Bethe H. A., 2001, New Astron., 6, 457
Bruenn S. W., 1985, ApJS, 58, 771
Bruenn S. W. et al., 2013, ApJ, 767, L6
Buras R., Rampp M., Janka H.-T., Kifonidis K., 2006, A&A, 447, 1049
Burrows A., 2013, Rev. Mod. Phys., 85, 245
Colgate S. A., White R. H., 1966, ApJ, 143, 626
Dall'Osso S., Piran T., Shaviv N., 2014, MNRAS, 438, 1005
Dolence J. C., Burrows A., Zhang W., 2015, ApJ, 800, 10
Drake A. J. et al., 2009, ApJ, 696, 870
Drout M. R. et al., 2011, ApJ, 741, 97
Drout M. R. et al., 2013, ApJ, 774, 58
Drout M. R. et al., 2014, ApJ, 794, 23
Foglizzo T. et al., 2015, PASA, 32, 9
Hanke F., Müller B., Wongwathanarat A., Marek A., Janka H.-T., 2013, ApJ, 770, 66
Herwig F., 2000, A&A, 360, 952
Janka H.-T., 2012, Annu. Rev. Nucl. Part. Sci., 62, 407
Kaiser N. et al., 2010, Proc. SPIE, 7733, 77330E
Keller S. C. et al., 2007, PASA, 24, 1
Kitaura F. S., Janka H., Hillebrandt W., 2006, A&A, 450, 345
Kotake K., Takiwaki T., Suwa Y., Iwakami Nakano W., Kawagoe S., Masada Y., Fujimoto S., 2012, Adv. Astron., 2012, 428757
Lattimer J. M., 2012, Annu. Rev. Nucl. Part. Sci., 62, 485
Lattimer J. M., Swesty F. D., 1991, Nucl. Phys. A, 535, 331
Law N. M. et al., 2009, PASP, 121, 1395
Liebendörfer M., Whitehouse S. C., Fischer T., 2009, ApJ, 698, 1174
Melson T., Janka H.-T., Marek A., 2015a, ApJ, 801, L24
Melson T., Janka H.-T., Bollig R., Hanke F., Marek A., Müller B., 2015b, ApJ, 808, L42
Miyazaki S. et al., 2012, Proc. SPIE, 8446, 84460Z
Moriya T. J., Tominaga N., Langer N., Nomoto K., Blinnikov S. I., Sorokina E. I., 2014, A&A, 569, A57
Nagataki S., Hashimoto M.-a., Sato K., Yamada S., 1997, ApJ, 486, 1026
Nakamura K., Takiwaki T., Kuroda T., Kotake K., 2014, preprint (arXiv:1406.2415)
O'Connor E., Ott C. D., 2011, ApJ, 730, 70
O'Connor E., Ott C. D., 2013, ApJ, 762, 126
Pejcha O., Thompson T. A., 2015, ApJ, 801, 90
Piran T., Shaviv N. J., 2005, Phys. Rev. Lett., 94, 051102
Podsiadlowski P., Langer N., Poelarends A. J. T., Rappaport S., Heger A., Pfahl E., 2004, ApJ, 612, 1044
Rau A. et al., 2009, PASP, 121, 1334
Scheck L., Kifonidis K., Janka H.-T., Müller E., 2006, A&A, 457, 963
Siess L., 2009, A&A, 497, 463
Stone J. M., Norman M. L., 1992, ApJS, 80, 753
Sukhbold T., Woosley S. E., 2014, ApJ, 783, 10
Suwa Y., 2014, PASJ, 66, L1
Suwa Y., Kotake K., Takiwaki T., Whitehouse S. C., Liebendörfer M., Sato K., 2010, PASJ, 62, L49
Suwa Y., Kotake K., Takiwaki T., Liebendörfer M., Sato K., 2011, ApJ, 738, 165
Suwa Y., Takiwaki T., Kotake K., Fischer T., Liebendörfer M., Sato K., 2013, ApJ, 764, 99
Suwa Y., Yamada S., Takiwaki T., Kotake K., 2014, preprint (arXiv:1406.6414)

Takahashi K., Yoshida T., Umeda H., 2013, ApJ, 771, 28
Takiwaki T., Kotake K., Suwa Y., 2014, ApJ, 786, 83
Tauris T. M., Langer N., Moriya T. J., Podsiadlowski P., Yoon S.-C., Blinnikov S. I., 2013, ApJ, 778, L23
Tauris T. M., Langer N., Podsiadlowski P., 2015, MNRAS, 451, 2123
Timmes F. X., Woosley S. E., Weaver T. A., 1996, ApJ, 457, 834
Tominaga N. et al., 2014, Astron. Telegram, 6291, 1
Ugliano M., Janka H.-T., Marek A., Arcones A., 2012, ApJ, 757, 69
Umeda H., Yoshida T., Takahashi K., 2012, Prog. Theor. Exp. Phys., 2012, 01A302
Wellstein S., Langer N., 1999, A&A, 350, 148
Wongwathanarat A., Janka H.-T., Müller E., 2013, A&A, 552, A126
Woosley S. E., Heger A., 2015, ApJ, 810, 34
Yoshida T., Okita S., Umeda H., 2014, MNRAS, 438, 3119

This paper has been typeset from a TEX/LATEX file prepared by the author.